Spectral Characteristics of Convective-Scale Precipitation Observations and Forecasts

MAY WONG AND WILLIAM C. SKAMAROCK

National Center for Atmospheric Research,[a] Boulder, Colorado

(Manuscript received 11 May 2016, in final form 19 July 2016)

ABSTRACT

As an alternative to traditional precipitation analysis and forecast verification, 1D and 2D spectral decompositions of NCEP/Stage IV and Multi-Radar Multi-Sensor (MRMS) precipitation products and convective-scale model forecasts are examined. Both the stage IV and MRMS analyses and the model forecasts show a similar weak power-law behavior in 1D spectral decompositions, although the MRMS analysis does not drop off in power at wavelengths less than approximately 20 km as found in the stage IV analysis. The convective-scale forecasts produce similar behavior to the MRMS when the forecast model's effective resolution is sufficient. Neither the MRMS analyses nor the forecasts suggest the existence of a break in the spectral slope at the scales for which the analyses and forecasts are valid. The 2D spectra of both observations and forecasts, expressed in terms of an absolute wavenumber and azimuthal angle, show power varying significantly as a function of azimuthal angle for a given wavenumber. This azimuthal anisotropy is significant, and is dominated by the second mode (wavenumber 2). The phase of the mode is the result of the orientation of precipitation features and, hence, convective system orientations and propagation. Observations show a shift in orientation (phase) over May–June–July. The convective forecasts reproduce this shift in phase, although with a consistent but small phase error.

1. Introduction

The expanding use of convection-permitting forecast models is one of the defining characteristics of the evolving numerical weather prediction (NWP) enterprise over the last few decades. Convection-permitting model configurations, involving grids with horizontal cell spacing of a few kilometers or less in which deep convective updrafts are explicitly simulated, produce convective-system structure and evolution very similar to what is observed. These high-resolution model configurations also allow for better representation of terrain and topographic flow effects, such as blocking, in addition to better representation of other atmospheric inputs arising from land use, etc. In research applications, convection-permitting simulations have been employed for many decades within regional configurations, and global convection-permitting models are beginning to be applied in research applications as computer and model capabilities grow. Operational NWP centers are increasingly employing convection-permitting models on the regional scale, and within the next decade it should be possible to employ convection-permitting global operational NWP models.

With the important emphasis on precipitation forecasting in NWP applications, there is an increasing need to develop precipitation analyses for both models and observations that take into account the increasingly smaller scales we are simulating and observing to examine and quantify the realism in convective precipitation forecasts. Traditional approaches for comparing precipitation forecasts to observations, such as equitable threat scores (ETS) and bias (Wilks 2011; Jolliffe and Stephenson 2003), do not provide any direct measure of the scale or structure of precipitation features. Gilleland et al. (2009) provide a comprehensive review of recent spatial verification methods that describe the scale dependence of precipitation structure and displacement errors in model forecasts (e.g., Davis et al. 2006; Roberts and Lean 2008; Harris et al. 2001). Scale in particular is an important consideration in forecast model performance;

---

[a] The National Center for Atmospheric Research is sponsored by the National Science Foundation.

Corresponding author address: May Wong, National Center for Atmospheric Research, P.O. Box 3000, Boulder, CO 80307-3000. E-mail: mwong@ucar.edu

DOI: 10.1175/MWR-D-16-0183.1

specifically, what scales are resolved in a model forecast, and are they resolved properly.

The focus of our study is to assess the performance of precipitation forecasts at different spatial scales, in particular the scale dependence of precipitation variability as compared with observations. As an alternative to the traditional precipitation analysis and forecast verification approaches, in this paper we examine 1D and 2D spectral decompositions of the National Centers for Environmental Prediction (NCEP)/Stage IV and Multi-Radar Multi-Sensor (MRMS) precipitation products and convective-scale model forecasts. The analyses are performed over the central U.S. region using observations and model forecasts from the period of the National Oceanic and Atmospheric Administration (NOAA) Hazardous Weather Testbed (HWT) Spring Experiment that took place during the month of May 2015, and the Plains Elevated Convection At Night (PECAN) experiment that took place from early June to mid-July 2015. Forecasts examined in this study are produced by the global Model for Prediction Across Scales (MPAS; Skamarock et al. 2012) using variable-resolution meshes to reach convection-permitting scales, and the regional Weather Research and Forecasting (WRF) Model.

The 1D spectra can be derived from 2D spectra from integration over one of the coordinates. Observational analyses using 1D spectra exhibit a power-law relationship for precipitation as a function of horizontal scale, and this relationship is consistent with the power-law relationship observed for the horizontal wind fields, specifically the kinetic energy. Within the context of the 1D spectral analyses, we consider a number of questions including the following: 1) do observations show any break in the power-law scaling and 2) do convection-permitting model forecasts reproduce the power-law scaling, and over what scales are the forecast spectra accurate? The smallest scale where observed power-law scaling holds is one definition of the effective resolution of a model configuration, usually evaluated using horizontal or vertical velocity spectra.

Information is lost, however, when 2D spectra is integrated to produce the 1D spectra. To recover some of this information about the structure of the precipitation fields, the 2D precipitation spectra are cast in polar coordinates (horizontal wavenumber, azimuth) and the characteristics of the spectra as a function of azimuth for a given wavelength are examined. We consider the azimuthal variance from the stage IV and MRMS observational analyses and from the MPAS forecasts, including the level of isotropy in the structure of the azimuthal variance, and we consider how the variance and structure of the precipitation fields evolve from late spring (May) through summer (July). The observed 2D precipitation spectra change noticeably over the 2.5-month period, and this change is also evident in the forecast spectra.

The paper is organized as follows. We begin in section 2 with a description of the analysis domains, the observational datasets, and the forecast models. In section 3 we describe the basis for our analyses—the spectral decompositions and analyses based upon them. Vertical velocity and horizontal kinetic energy results from the spectral analyses are given in section 4, followed by those for precipitation in section 5. Spectral anisotropy of precipitation is examined in section 6. A summary is provided in section 7.

2. Description of models and observations

a. Analysis domains and time periods

We focus our spectral analyses over the central United States where midlatitude continental convection is most active during the forecast periods. Temporally averaged vertical velocity, horizontal kinetic energy, and precipitation spectra are computed from hourly forecasts and precipitation analyses over a domain with 720×720 grid points (1800×1800 points for the MRMS analyses) (shown in red in Fig. 1). In a case study, we run WRF simulations over smaller forecast domains and the analysis domain is reduced to 560×560 grid points (orange) for a 3-km simulation, and 796×796 grid points (blue) for a 1-km simulation.

For all domains, we compute the spectra over a region as large as possible while remaining sufficiently far from topographically driven features (such as precipitation formation over the Rockies) that may dominate and mask the spatial characteristics of convective precipitation. When defining an analysis domain, we avoid including any cells within regions of mesh refinement or lateral boundary relaxation in MPAS and WRF, respectively. The larger analysis domains also help prevent overpenalizing the convection-permitting forecasts due to small spatial or temporal offsets.

For all model output and observations, we interpolate variables from their native grids to a regular latitude–longitude grid. For MPAS and stage IV gridded output, fields are interpolated to a $0.025° \times 0.025°$ grid ($\Delta x \approx 2.8$ km and $\Delta y \approx 2.2$ km). The MRMS 1-km gridded output exists on a $0.01° \times 0.01°$ grid ($\Delta x \approx 1.1$ km and $\Delta y \approx 0.9$ km). The WRF 3- and 1-km model output are interpolated onto the 0.025° and 0.01° grids, respectively, from its native Lambert conformal grid. Over the analysis region, the change in grid cell spacing is relatively small, and Fourier analysis is carried out on these interpolated fields.

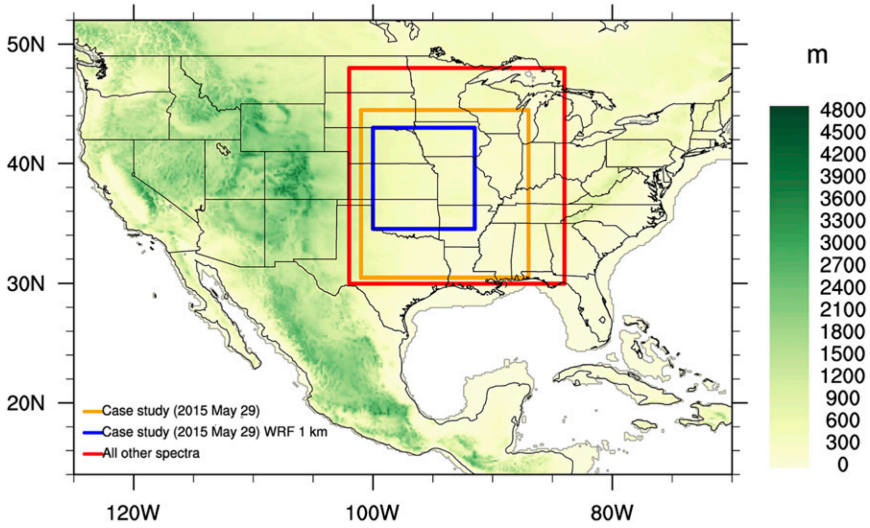

FIG. 1. Geographical domains used in the spectral analysis. Filled contours show topography elevation (m).

Two sets of experimental MPAS convective forecasts over the continental United States define the analysis time periods. The first set of forecasts is produced as a part of the HWT Spring Experiment that was conducted by the MPAS group at the National Center for Atmospheric Research (NCAR). Between 1 and 31 May, daily 5-day (120 h) forecasts were produced and initialized by the 0000 UTC Global Forecast System (GFS) analysis made available operationally by NCEP. The second set of forecasts was generated for the period of the PECAN field campaign. The 3-day (72 h) forecasts were produced daily between 8 June and 14 July (also initialized by the operational 0000 UTC GFS analysis).

b. *Stage IV 4-km gridded precipitation estimates*

NCEP provides a national precipitation analysis product using regional hourly and 6-hourly multisensor precipitation analyses from the 12 National Weather Service River Forecast Centers (RFC) over the continental United States. These routine analyses are based on WSR-88D observations bias corrected using rain gauge measurements and satellite information; there is also some manual quality control by forecasters at the RFCs. Upon receiving the RFC analyses, NCEP then conglomerates the information onto a national 4-km grid resulting in the stage IV product (Lin and Mitchell 2005).

c. *MRMS 1-km gridded precipitation estimates*

An MRMS system, developed at the National Severe Storms Laboratory, was recently implemented at NCEP (Zhang et al. 2014, 2016). This system provides gridded precipitation estimates over the continental United States at 1-km grid spacing. The product is generated by combining information from multiple radars in the United States and Canada, lightning and rain gauges, climatology data, satellite data, atmospheric environmental data, and NWP model output. Unlike the stage IV precipitation estimates, the MRMS estimates are fully automated and do not benefit from manual quality control. We obtain hourly accumulated MRMS precipitation estimates via the archive on the Iowa Environmental Mesonet (IEM).[1] (A graphical user interface for the MRMS products is available online at http://mrms.ou.edu.)

d. *MPAS*

MPAS is a global nonhydrostatic atmospheric model using a spherical centroidal Voronoi mesh and model governing equations discretized on a C grid (Skamarock et al. 2012). The unstructured centroidal Voronoi mesh allows for local refinement on the sphere through the use of a variable-resolution mesh. Such a mesh may be beneficial for removing numerical artifacts due to lateral boundary conditions in traditional two-way nested models. Here we examine spectral characteristics of convection-permitting forecasts produced by a variable-resolution MPAS. Two mesh configurations were used: (i) 50–3 km for the HWT forecasts and (ii) 15–3 km for the PECAN forecasts, which contained approximately 6.85 and 6.5 million cells, respectively. The latter configuration is

---

[1] Available online at https://mesonet.agron.iastate.edu.

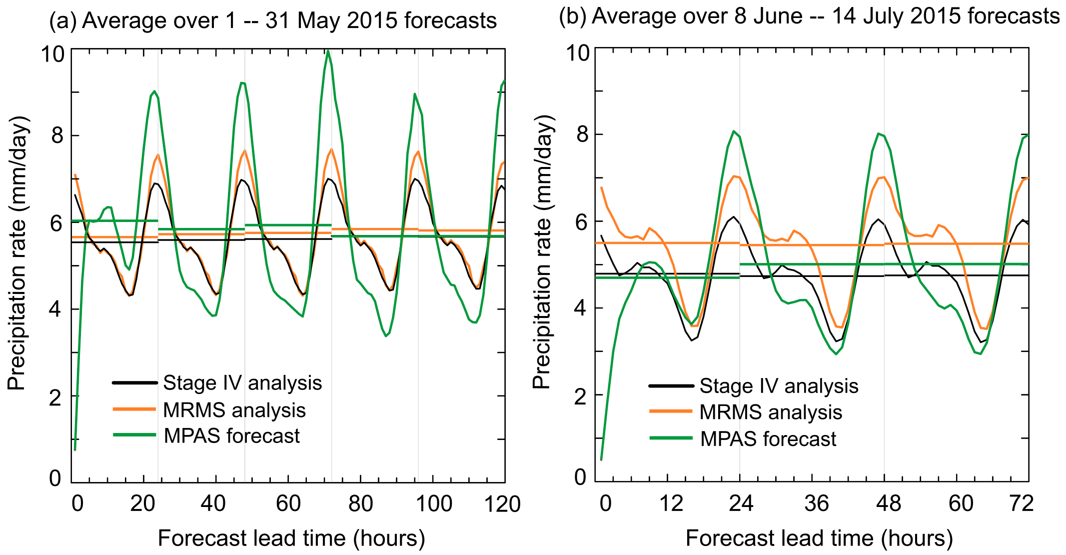

FIG. 2. Average hourly precipitation rate (mm day^{-1}) as a function of forecast lead time (h) over the central United States from MPAS (green), stage IV (black), and MRMS (orange) for the two experimental convection-resolving forecast periods: (a) HWT during May 2015 and (b) PECAN field campaign (June–July 2015). Horizontal lines show the average hourly precipitation rate over each forecast day.

computationally less expensive albeit with a higher horizontal resolution outside of the refined region because there are slightly fewer cells in the refined region with nominally 3-km horizontal grid spacing.

Both sets of forecasts used the same physics suite adapted from the Advanced Research version of the Weather Research and Forecasting (WRF-ARW) Model (Skamarock et al. 2008). The following physics options were used: Mellor–Yamada–Nakanishi–Niino (MYNN) surface layer scheme (from WRF 3.5) and planetary boundary layer (PBL) scheme (from WRF 3.6.1; Nakanishi and Niino 2009), the Grell–Freitas scale-aware cumulus scheme (modified from WRF 3.6.1; Grell and Freitas 2014), the WSM6 single-moment microphysics scheme (with prognostic variables for cloud liquid-water, cloud ice, rainwater, snow, and graupel; from WRF 3.5; Hong and Lim 2006), and the Rapid Radiative Transfer Model for GCM (RRTMG) short- and longwave radiation schemes (from WRF V3.4.1; Mlawer et al. 1997; Iacono et al. 2000).

Figure 2 shows the MPAS, stage IV, and MRMS average hourly precipitation rate as a function of forecast lead time over the largest analysis domain for the two forecast periods. To avoid model spinup errors, such as that discussed in Skamarock (2004), we do not use the first 24 forecast hours in our spectral calculations. MPAS typically overestimates the diurnal precipitation maximum and underestimates the minimum, but the model bias does not vary significantly with forecast lead time. Therefore, we can use all hourly forecasts beyond spinup to improve the statistical robustness of the spectral calculations.

e. WRF-ARW

In a case study, the regional WRF-ARW is used to generate a 48-h forecast at 3- and 1-km horizontal grid spacings. The 3-km forecast is two-way nested within a 15-km parent domain, initialized from analyses generated by the WRF Data Assimilation Research Testbed (WRF/DART using V3.6.1). The WRF/DART is a continuously cycled system that uses an ensemble adjustment Kalman filter and observations from aircraft, marine, surface, and upper-air observations. The 15–3-km model configuration follows the NCAR Ensemble Forecast System (EFS) [see Schwartz et al. (2015) for more details]. The 3-km forecast is then one-way-nested to produce the 1-km forecast.

The following physics suite is used in these forecasts: the Mellor–Yamada–Janjić (MYJ) PBL scheme (Mellor and Yamada 1982; Janjić 1994, 2002) with the Eta surface layer scheme, Tiedtke cumulus scheme (Tiedtke 1989; Zhang et al. 2011) (no cumulus parameterization is used for the 3- and 1-km domains), Thompson microphysics scheme (Thompson et al. 2008) (with prognostic variables for cloud liquid-water, pristine ice, rainwater, snow, and graupel), and the RRTMG short- and longwave radiation schemes (Mlawer et al. 1997; Iacono et al. 2000) with aerosol and ozone climatologies. Similar to the MPAS forecasts, we eliminate the first 24 h of forecasts in calculating the spatial spectra.

3. Spectral power analysis

a. 2D power spectrum

The power spectra are generated using two-dimensional Fourier transforms. In contrast to a gridpoint to gridpoint evaluation, comparing temporally averaged power spectra gives an alternative objective assessment of the modeled spatial features with observations. By retaining the spectra's dimensionality, one can obtain additional information on the spatial orientation of these features. In this study, we utilize two-dimensional spectral information to assess model behavior over a range of spatial scales (from large/synoptic- to near-grid scales).

The Fourier transform algorithm assumes periodicity in the input field. We have tested two different techniques to circumvent the aperiodicity of our domain. One is a detrending technique as described in Errico (1985); the other is a Hanning window [e.g., as described in Harris (1978)], which is essentially a spatial cosine-bell filter that gradually reduces the field from its full value at the center of the domain to zero at the boundaries. The 2D Hanning window is applied by scaling each grid point (m, n) of a two-dimensional physical field with the following coefficient:

$$c(m,n) = \left\{\frac{1}{2} - \frac{1}{2}\cos\left[\frac{2\pi(m-1)}{N_x - 1}\right]\right\} \times \left\{\frac{1}{2} - \frac{1}{2}\cos\left[\frac{2\pi(n-1)}{N_y - 1}\right]\right\},$$

where N_x and N_y are the number of grid points in the x and y directions, respectively.

In terms of the 1D spectra, the resulting spectral slopes from the two techniques are very similar, but the Hanning window generally reduces the overall power. The detrended fields, however, usually contain patterns of lines (due to the linear detrending computed at each row and column separately). Although this does not affect the resulting 1D spectrum (e.g., Blažica et al. 2015), objective interpretation of the 2D spectrum becomes difficult when lines of power peaks are reflected along $k_x = 0$ and $k_y = 0$. For this reason, despite the power reduction, we apply the Hanning window in all of our 2D spectral analyses. The comparisons of spectral power and slopes between modeled and observed fields remain valid since we apply the same Hanning window.

b. 1D power spectrum

Examining the power at the spectral tail near the grid scale can provide some insight on the model-effective resolution (Skamarock 2004). To obtain a 1D rainfall spectrum, past studies (e.g., Crane 1990; Harris et al. 2001; Morales and Poveda 2009; Parodi et al. 2011; Willeit et al. 2015) have used the detrending technique followed by azimuthal averaging of the 2D spectrum. Our 1D rainfall spectra (both simulated and observed) are computed in a manner consistent with these previous studies. Azimuthal averaging returns a flat spectrum when the signal is white noise and is useful for interpreting spatial correlation in the field, whereas azimuthal integration returns a spectrum with a constant spectral slope. We also examine simulated 1D horizontal kinetic energy and vertical velocity spectra; for these spectra, the Hanning window followed by azimuthal integration is used.

c. Spectral power anisotropy

Previous studies on rainfall spectra have largely focused on 1D spectra (e.g., Crane 1990; Harris et al. 2001; Morales and Poveda 2009; Parodi et al. 2011; Willeit et al. 2015). As mentioned earlier, 2D spectra retain information such as the orientation of dominant features at each spatial scale that are unavailable from 1D spectra alone. Here, in addition to 1D spectra, we also examine 2D rainfall spectra to objectively identify the orientation and structure of dominant precipitation features. Elongated precipitation features are reflected as anisotropy in the 2D power spectrum. Hinkelman et al. (2005, 2007) have defined a measure to quantify such horizontal spectral anisotropy but for determining elongated cloud fields. Their measure depends on the geometry of the 2D spectrum. We propose a similar anisotropy parameter but using the ratio of power variance to the squared mean at each total wavenumber k, defined as

$$p_\theta(k) = \sigma_\theta^2(k)/\mu_\theta^2(k),$$

where $\sigma_\theta(k)$ and $\mu_\theta(k)$ are the standard deviation and azimuthal average, respectively, of the power coefficients $S(k, \theta)$ at wavenumber k. The normalization using μ_θ^2 reduces the parameter range, which would otherwise span many orders of magnitude due to the large differences in power between each wavenumber. The normalization also highlights the variance due to anisotropy rather than noise. For an isotropic spectrum, $S(k, \theta) = S(k)$ and $\sigma_\theta(k) = 0$.

Next we define an anisotropy phase $\phi'(k)$ to quantify the dominant orientation of anisotropy. The Fourier transform of a real-valued two-dimensional field is symmetric about $k_x = -k_y$. If the 2D spectrum shows a peak in power along a particular angle θ, the power at an arbitrary total wavenumber will be in the form of two sinusoidal waves with a phase shift depending on θ at

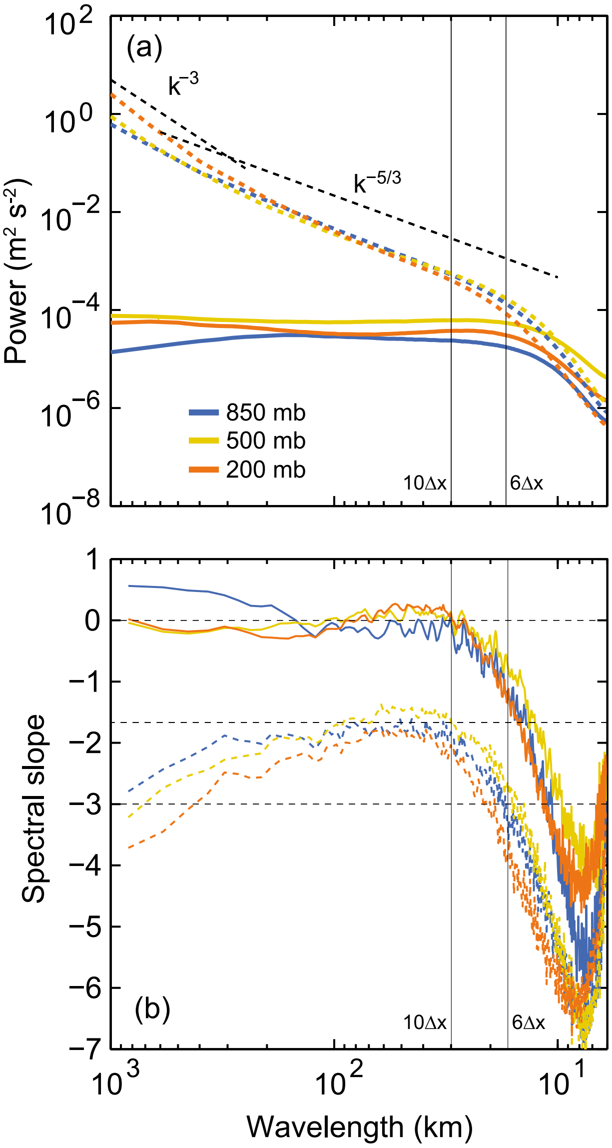

FIG. 3. (a) Spectra and (b) spectral slopes of MPAS horizontal kinetic energy (dashed lines) and vertical velocity (solid lines) over the central United States at 850 (blue), 500 (yellow), and 200 hPa (orange). Spectra are temporal averages over both the HWT and PECAN forecast periods.

which the peak occurs. To quantify this phase shift, we perform a 1D Fourier transform on $S(k_0, \theta)$ for all wavenumbers k_0 and find the phase angle $\phi(k_0)$ of the second harmonic, where $-\pi \le \phi(k_0) \le \pi$. We then map the phase angle ϕ to the anisotropy phase ϕ' using

$$\phi' = \begin{cases} -\phi/2 & \text{if} \quad \phi \le 0 \\ \pi - \phi/2 & \text{if} \quad \phi > 0, \end{cases}$$

such that $\phi'(k) = 0$ corresponds to $(k_x, 0)$ in the 2D spectrum and the angle increases counterclockwise. The heaviest rainfall feature will align perpendicular to this phase; for example, an elongated rainfall feature aligned in the northeast–southwest direction will show anisotropy at $\phi' = 3\pi/4$ in the 2D spectrum.

4. Vertical velocity and horizontal kinetic energy

We first present 1D horizontal kinetic energy and vertical velocity spectra from MPAS over the largest analysis domain (Fig. 3). The plotted spectra are temporal averages of all hourly spectra from both the HWT and PECAN forecasts. Similar to past observations (e.g., Nastrom et al. 1984; Nastrom and Gage 1985; Julian et al. 1970; Cho and Lindborg 2001), the $k^{-5/3}$ and the k^{-3} spectra are reproduced by the model at three pressure levels: 850, 500, and 200 hPa (dashed lines in Fig. 3). We found only small differences in the spectral slopes among the three monthly spectra from differing weather conditions and sample sizes (not shown). At wavelengths greater than approximately 400 km, the slopes in the kinetic energy spectra at all three levels are shallower than −3, as was also found in the global MPAS troposphere and stratosphere spectra presented in Skamarock et al. (2014). The spectrum in the k^{-3} regime at 850 hPa shows a gentler slope than those at 500 and 200 hPa, consistent with past observational and modeling studies (e.g., Julian et al. 1970; Horn and Bryson 1963; Wiin-Nielsen 1967; Hamilton et al. 2008; Ricard et al. 2013). The slopes at the mesoscale (wavelengths between approximately 25 and 400 km) correspond well to the theoretical −5/3 slope up to a wavelength of $10\Delta x$, where a departure from the −5/3 slope may be interpreted as reaching the model-effective resolution (Skamarock 2004). This effective resolution is smaller than the global average of $6\Delta x$ found in Skamarock et al. (2014) and may be a result of the dominant local weather regime (continental convection) examined in this study.

The vertical velocity spectra at pressure levels 850, 500, and 200 hPa are shown in solid lines in Fig. 3. Flat vertical velocity spectra were also observed in the stratospheric aircraft measurements (e.g., Bacmeister et al. 1996) and model simulations (e.g., Terasaki et al. 2009; Bierdel et al. 2012; Langhans et al. 2012; Skamarock et al. 2014; Stephan and Alexander 2015). The spectra exhibit a flat shape up to a wavelength of approximately $10\Delta x$. There appears to be a weak spectral peak near wavelength 30 km (as indicated by positive slopes in Fig. 3b); interestingly, the stratospheric measurements presented in Bacmeister et al. (1996) (with a wavelength resolution of about 200 m) also showed a deviation from a flat spectrum at about 25 km. However, since this is near the filter scale of the model (where the kinetic energy spectra deviate from $k^{-5/3}$), it

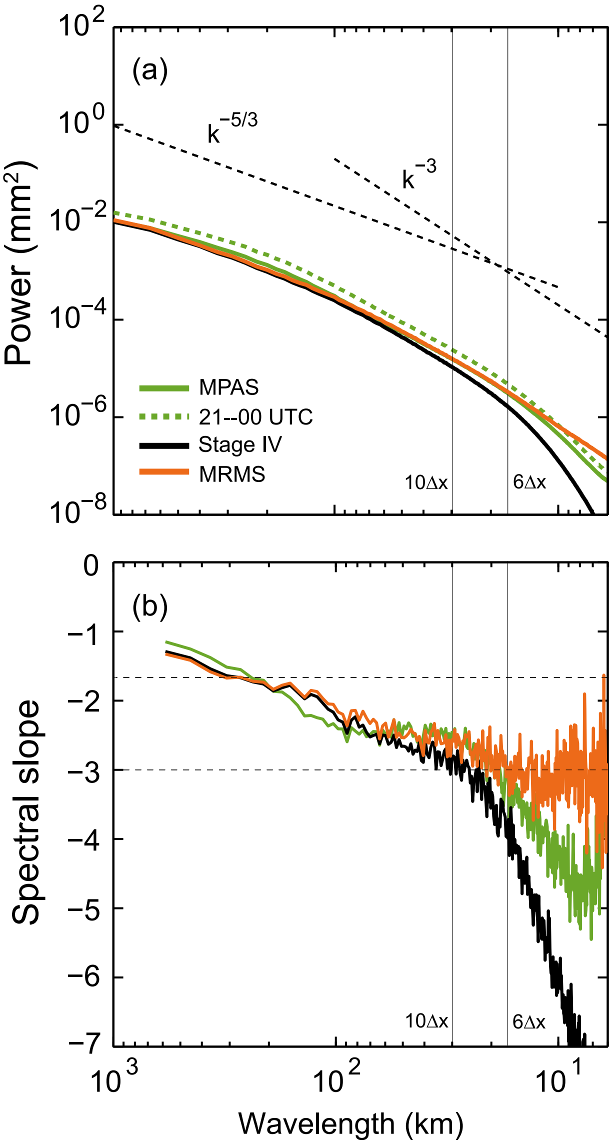

FIG. 4. (a) Spectra and (b) spectral slopes from MPAS (green), stage IV (black), and MRMS (orange) hourly rainfall accumulations. Spectra are temporal averages over both the HWT and PECAN forecast periods. Dashed line shows the MPAS spectrum averaged over all 2100–0300 UTC forecasts, when convection is most active from the late afternoon to early evening. Spectral slopes are smoothed using a running average.

is unclear whether the weak spectral peak is due to physical or marginally resolved processes. The model resolution is still too low to accurately resolve the spectral characteristics of convective vertical velocities (Bryan et al. 2003).

5. Precipitation scaling near the grid scale

Some past studies (e.g., Crane 1990; Harris et al. 2001; Willeit et al. 2015) have found distinct breaks in the spectral slope at the 15–30-km wavelengths in 1D rainfall spectra based on radar observations. Crane (1990) computed rainfall spectra using 1-km horizontal grid spacing radar volume scans just below the freezing level. He found three scaling regimes: a $k^{-5/3}$ regime at scales between 13.5 and 50 km, a k^{-3} regime at scales between 4 and 13.5 km, and a k^{-1} regime below 4 km. He attributed the $k^{-5/3}$ and k^{-3} scalings to an energy input at the 13.5-km scale and a departure of the two-dimensional turbulence theory at the 4-km scale. Others, however, have found more consistent scaling (i.e., no break in the spectral slope) at scales smaller than 30 km. Menabde et al. (1999) examined the scaling between 500 m and 30 km using radar scans with 250-m resolution pixels and found spectral slopes in the range of $k^{-2.11}$ to $k^{-2.42}$. Harris et al. (2001) examined rainfall spectra from a 2-km horizontal grid spacing radar and found scaling from $k^{-2.7}$ to $k^{-3.1}$ at the 4–33-km scales, transitioning to a much gentler slope at scales greater than 33 km (at approximately k^{-1} but there was little mentioning of this scaling).

Harris et al. (2001) also conducted a 3-km numerical simulation. In addition to a break at 33 km, they also found a spectral break at 15 km ($5\Delta x$) in their model results and attributed the spectral drop to numerical filter effects. Willeit et al. (2015) compared rainfall spectra from 1-km radar observations with those from 2.8-km model simulations. They found that for convective events, the observed spectra showed a scaling break at about 15–20 km, whereas the modeled spectra showed a break at 20–30 km, with a slope ($k^{-2.21}$) gentler than observed ($k^{-3.16}$ for 1-h rainfall accumulations and $k^{-2.72}$ for rainfall rate) at the smaller scales (5.6–25 km).

These past studies found a range of fitted slope values in their observed spectra between $k^{-2.11}$ and $k^{-3.1}$ for rainfall rates, and slightly steeper slopes for 1-h averages. Each study differs in their radar locations, duration, and reflectivity-to-rainfall rate conversion. Moreover, all the aforementioned studies used reflectivity from different radars, where radar-rainfall estimates are subject to uncertainties such as range effects due to beam elevation and attenuation, and choice of a single Z–R relationship (Wilson and Brandes 1979). Using single radar measurements also means that the domain is limited by the maximum range and azimuthally averaged spectral estimates at scales greater than 15 km may be affected by a smaller sample size (Crane 1990). To avoid these issues, we use observed rainfall accumulations from multisensor precipitation estimates, which utilize a dense network of rain gauges to bias adjust radar-rainfall estimates (among other adjustment measures such as satellite estimates). Over our region of interest in the central

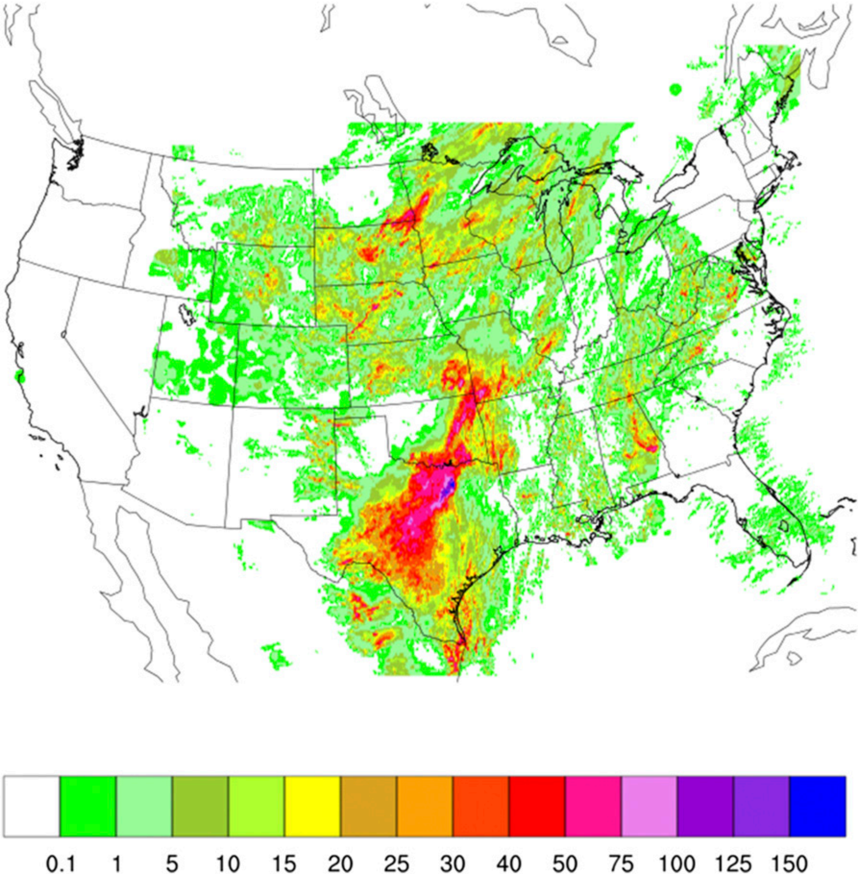

FIG. 5. Stage IV accumulated precipitation (mm) from 0000 UTC 29 May to 0000 UTC 30 May 2015.

United States, there is also a dense radar network with some overlapping coverage allowing our domain to be much larger than those used in the past studies.

Figure 4 shows the 1D rainfall spectrum from MPAS hourly accumulations compared with those from NCEP/Stage IV and MRMS. At scales greater than about 40 km, the magnitudes from MPAS show similar scaling behavior as those from stage IV and MRMS. The dashed green line shows the MPAS spectrum from the diurnally convective hours (between 2100 and 0300 UTC). The shape of the spectrum is unchanged (similarly for stage IV and MRMS; not shown). Near the grid scale, the power from stage IV analyses drops off much faster with wavenumber than those from MPAS and MRMS. The steeper (more negative) spectral slope indicates that stage IV small-scale precipitation features are smoother and more organized. The higher-resolution MRMS, on the other hand, shows continued scaling at approximately k^{-3} down to 6 km, in rough agreement with those found in past studies. The rainfall spectrum from MPAS compares well with MRMS and shows similar small-scale variability down to approximately 12 km, although the slopes begin to differ noticeably at about $6\Delta x$ [similar to the results found in Harris et al. (2001) for their model].

To examine the effect of model horizontal resolution on the near-grid-scale scaling behavior, we conducted WRF 3- and 1-km forecasts for a 48-h period beginning at 0000 UTC 28 May 2015. During this period, a squall line developed over the elevated terrain of New Mexico, and propagated eastward, sweeping through northwestern Texas, with peak precipitation amounts occurring between 0000 and 0500 UTC 29 May 2015. Scattered thunderstorms then lingered over much of eastern Oklahoma, Arkansas, and Missouri between 2100 UTC 29 May and 1200 UTC 30 May 2015. The distribution of 24-h accumulated precipitation from stage IV is shown in Fig. 5.

The rainfall spectrum (hourly accumulations) and slope for the 24-h period are shown in Figs. 6a and 6b, respectively. Similar to the 4-km stage IV spectrum, the WRF 3-km simulation shows a sharp spectral drop at the 6–25-km wavelengths, whereas both the 1-km WRF forecast and MRMS analysis show relatively consistent scaling down to 6 km. The lack of a sharp spectral drop in

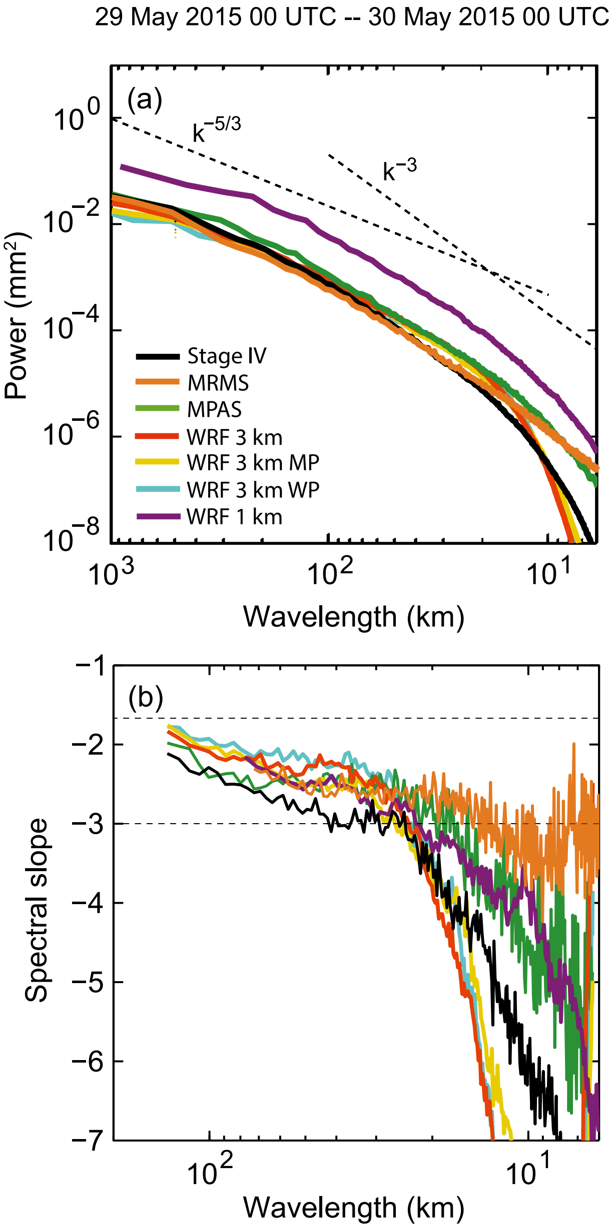

FIG. 6. (a) Spectra and (b) spectral slopes of modeled and observed hourly accumulated rainfall (mm) during forecast hours 24–48 initialized at 0000 UTC 28 May 2015. Analysis domain of the WRF 1-km simulation is smaller than the others. Spectral slopes are smoothed using a running average.

the higher-resolution forecast and analysis indicates that the drop in the 3-km WRF forecast and the 4-km stage IV spectra may be due to the coarser resolution in WRF and smoothing procedures in the objective analyses. The MPAS spectral slopes show closer resemblance to the WRF 1-km forecast than MRMS.

The WRF 3-km forecasts use a different set of physics options than in the 3-km MPAS forecasts. We conducted two additional 3-km WRF simulations with the WRF physics (WP) suite and the MPAS physics (MP) suite. These 3-km domains (of 581 × 581 grid points) are smaller than that used previously, but are initialized in the same fashion. The power spectra from these WRF 3-km forecasts are shown in Figs. 6a and 6b. We note that slightly less precipitation is formed in these forecasts, a consequence of lateral boundary effects using a smaller domain. Differences are found between the two sets of physics parameterizations at the synoptic scale, but near the grid scale their spectral behavior is very similar (and also similar to that of the previous WRF 3-km forecast). We can, therefore, conclude that the spectral drop at the grid scale is independent of physics options.

The 1-km results, using both models and observations, suggest that the spectral drop seen in the stage IV analyses is most likely related to its resolution and the density of the rain gauges used for bias correction. The higher-resolution MRMS analyses are bias corrected using twice as many in situ precipitation observations from approximately 10 000 rain gauges (Zhang et al. 2016), and their spectra do not exhibit this drop.

Finally, we note that there are differences between the numerical filters for scalars in MPAS and WRF that may affect the near-grid-scale behavior. In MPAS, no explicit diffusion is applied on the scalar variables, but the third-order advection scheme has a fourth-order damping term and a monotonicity constraint in the scalar advection scheme behaves like a filter (Skamarock et al. 2012). In WRF, a fifth-order horizontal advection scheme is used, which is inherently diffusive with a sixth-order damping term. In addition to monotonic moisture advection, a sixth-order hyperdiffusion is employed for scalars (Knievel et al. 2007). When examining the two models' vertical velocity and horizontal kinetic energy spectra, similar behavior (but to a lesser effect than for precipitation) is found near the grid scale, with the vertical velocity spectra showing larger differences in the spectral slopes than in the kinetic energy spectra. A WRF-MP simulation without any sixth-order diffusion indicates that the explicit hyperdiffusion in WRF partially explains the difference in behavior. The kinetic energy spectral slopes are found to be much closer to those from MPAS, but some differences remain in the precipitation and vertical velocity spectra (especially at 500 hPa). Other factors that may affect the near-grid-scale behavior include the different model levels used and the more isotropic nature of the MPAS mesh, both of which warrant further investigation.

6. Orientation of dominant precipitation features

Figure 7 shows stage IV gridded analyses of 6-h rainfall accumulation on two different days: 1200 UTC 8 July 2015 (Fig. 7a) and 1200 UTC 28 May 2015 (Fig. 7b). Their

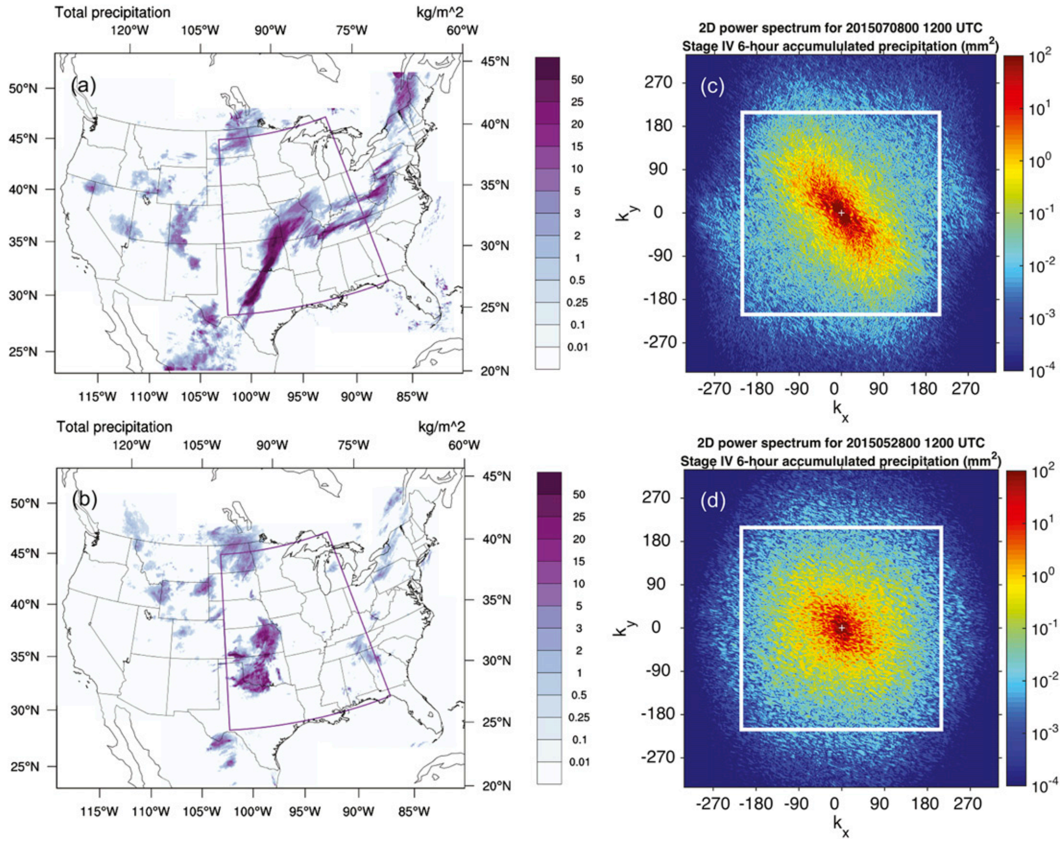

FIG. 7. Stage IV 6-h accumulated precipitation analyses for (a) a squall-line case at 1200 UTC 8 Jul 2015 and (b) a scattered thunderstorms case at 1200 UTC 28 May 2015 (purple boxes indicate the analysis domain), and (c),(d) their corresponding 2D power spectra (mm^2). White boxes indicate $2\Delta x$ of the stage IV grid (where $\Delta x \approx 4.75$ km).

power spectra are shown in Figs. 7c and 7d, respectively. In Fig. 7a, a linear squall line oriented in the northeast–southwest direction passed through the analysis region. Most of the power resides at the synoptic scale, where wavenumbers 1–20 represent wavelengths between 100 and 2000 km (note the logarithmic color scale). In the spectrum from the first case (Fig. 7c), the orientation of the squall line is reflected clearly as peaks in the power spectrum along an angle perpendicular to the physical feature. In the second case (Fig. 7b), precipitation events occurred in the form of scattered and less-organized convective cells. These systems resulted in a spectrum that is much more isotropic (Fig. 7d).

Figure 8 shows the 2D spectra from MPAS, stage IV, and MRMS averaged over three different extended periods. They all show similar variation in the orientations of the dominant warm-season precipitation features with time. The orientations of the physical features are predominantly in the northeast–southwest direction ($\phi' = 3\pi/4$) during May (top row) and transitioning to an east–west direction ($\phi' = \pi/2$) during June and July (middle and bottom rows, respectively).

Since the spectrum is symmetric, only even harmonics of the power along the azimuth are nontrivial. We examined the variance contributions of the second and fourth harmonics in the spectra shown in Fig. 8, and found that the second harmonic contributes 46.6%–62.2% of the variance, while the fourth harmonic only contributes 9.3%–14.5%. The phase shifts of the second harmonic are, therefore, used to compute the anisotropy phases in Fig. 9. It is interesting that at scales smaller than approximately 100 km, the model consistently overestimates the phase, consistent with Fig. 8. Near the grid scale, the anisotropy phases decrease sharply in stage IV, which is associated with reaching the Nyquist wavenumber (at a wavelength of 9.5 km).

There is a clear indication of a slow clockwise rotation from May to July. These dominant orientations are consistent with the frequently observed springtime mesoscale convective systems with well-defined squall lines that orient in the northeast–southwest direction. During late June and into July, nocturnal convection becomes more active and persistent ''heavy precipitation corridors'' confined within a narrow latitudinal band of 3°–4° are frequently observed in the region (Carbone et al.

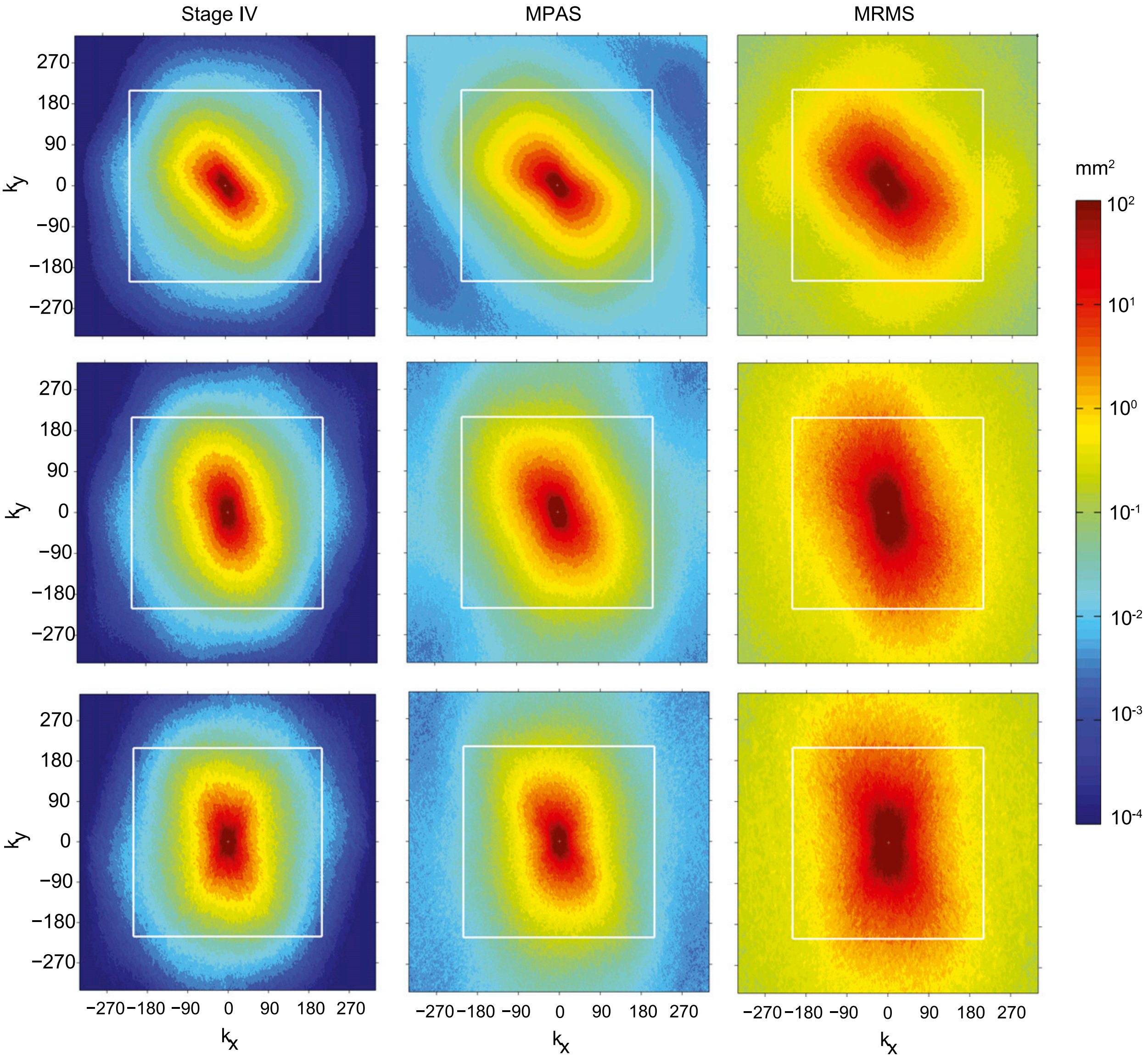

FIG. 8. Two-dimensional power spectra (mm^2) of 6-h accumulated rainfall from (middle column) MPAS forecasts initialized on (top) 1–31 May 2015, (middle) 8–30 Jun 2015, and (bottom) 1–14 Jul 2015, and the corresponding spectra from (left) stage IV and (right) MRMS analyses. The 2D power spectra are truncated at the 6-km wavelength. White boxes indicate 2Δx of the stage IV grid (where $\Delta x \approx 4.75$ km).

2002; Tuttle and Davis 2006). MPAS is able to reproduce the spectral anisotropy well in May and July, but with an underestimation in June (Fig. 10). The underestimation indicates that the MPAS spectrum is slightly more isotropic than those from stage IV and MRMS, and that the predicted precipitation features were less organized than observed.

7. Summary

We investigated the spectral properties of two national precipitation estimate products, the NCEP/Stage IV and MRMS analyses, which are based on multiple radars and in situ observations. These products are used to evaluate the precipitation forecasts from the global variable-resolution MPAS and the regional WRF over the central United States. Characteristics of 1D and 2D spectra of convective precipitation from observations and models are used to identify structural differences at various spatial scales.

The 1D precipitation spectrum based on stage IV analyses shows a distinct break in the spectral slope at approximately 25 km. The steeper slope at the smaller scales implies smoother and more organized precipitation

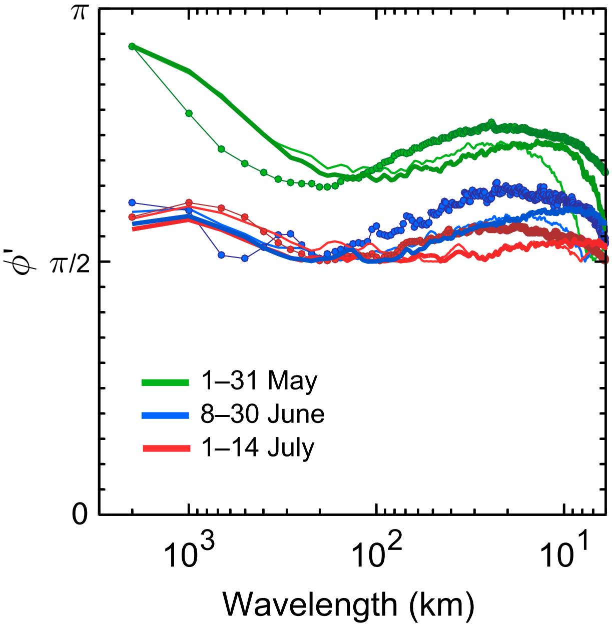

FIG. 9. Anisotropy phases of the 6-h accumulated precipitation spectra for MPAS (lines with circle markers), stage IV (thin solid lines), and MRMS (thick solid lines). Colors indicate spectra averaged over forecast periods initialized on 1–31 May (green), 8–30 Jun (blue), and 1–14 Jul 2015 (red).

structures. On the other hand, the MRMS spectrum shows near uniform scaling at k^{-3} between 6 and 100 km. The scale break in stage IV appears to be a result of the horizontal resolution, where finescale structures are likely smoothed out by the analysis procedure and limited by the density of the in situ observations. MPAS at a 3-km nominal grid spacing shows better agreement with the MRMS results, whereas the regional WRF at the same nominal grid spacing shows a similar scale break as that from stage IV. At a 1-km grid spacing, however, the WRF spectrum shows scaling similar to MRMS. Additional simulations indicate that the differences are not sensitive to physics options. MPAS is able to reproduce the small-scale variability observed in the MRMS analysis down to 12 km (≈4Δx).

By examining the full 2D average spectra, dominant precipitation orientations and structures are identified from the model and observations. Two statistical measures, an anisotropy phase and an anisotropy parameter, are used to quantify the orientation and structure of precipitating systems. These measures characterize the precipitation structure at various spatial scales and set aside differences in magnitude. MRMS, stage IV, and MPAS all show dominant features aligned in the northeast direction during the month of May, gradually shifting to an east–west direction in June and July, although MPAS tends to underestimate the phase angles.

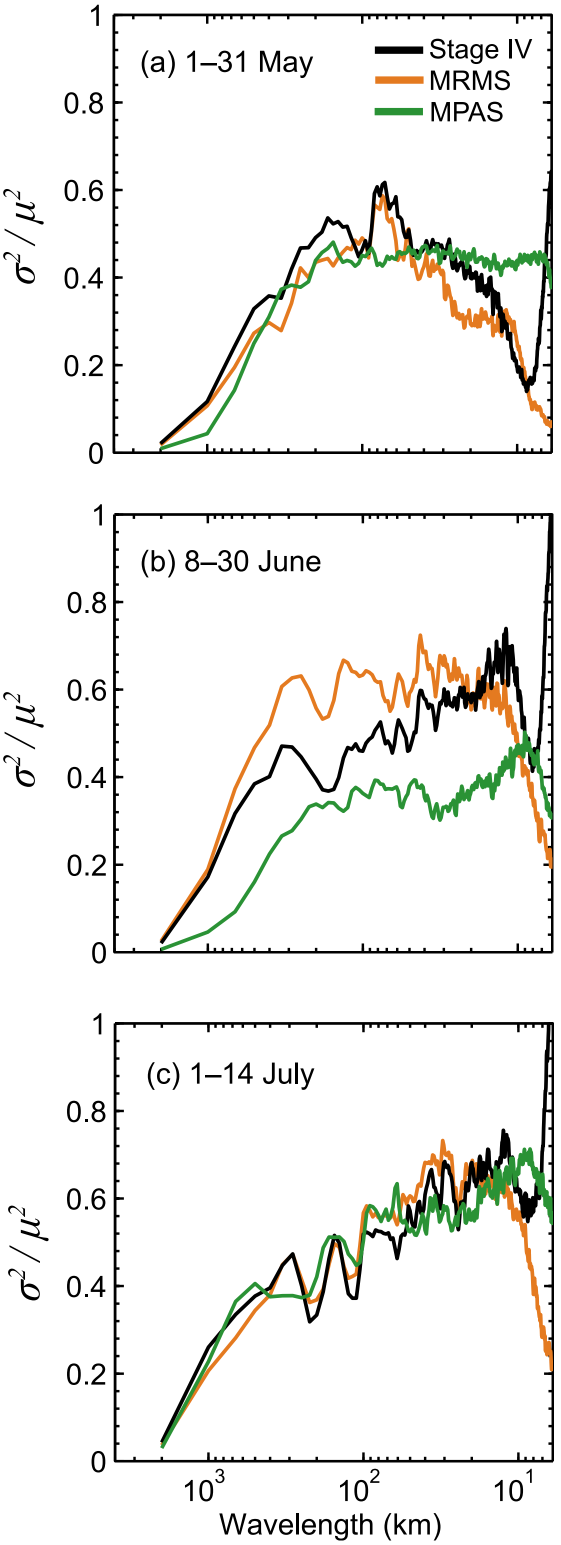

FIG. 10. Anisotropy parameter computed from the 6-h accumulated rainfall spectra from MPAS (green), stage IV (black), and MRMS (orange) over forecast periods initialized on (a) 1–31 May, (b) 8–30 Jun, and (c) 1–14 Jul 2015.

The shift in the orientation in the June and July forecasts is likely associated with rainfall corridors confined within a latitudinal band as frequently observed during the late summer over the Great Plains. The anisotropy parameter is used as a measure of the frequency of structured events. Well-organized systems such as squall lines have a larger anisotropy parameter, whereas more spatially sporadic thunderstorms have a smaller value. In this respect, MPAS agrees fairly well with stage IV except in June, where the forecast precipitating systems appear to be somewhat more disorganized.

Acknowledgments. We would like to acknowledge high-performance computing support from Yellowstone (ark:/85065/d7wd3xhc) provided by NCAR's Computational and Information Systems Laboratory, sponsored by the National Science Foundation. NCEP/Stage IV data are provided by NCAR/EOL under sponsorship of the National Science Foundation (http://data.eol.ucar.edu/). We thank Laura Fowler for developing the physics in MPAS, and David Ahijevych, George Bryan, Michael Duda, Kevin Manning, and Glen Romine for their help with various aspects of the analysis.

REFERENCES

Bacmeister, J. T., S. D. Eckermann, P. A. Newman, L. Lait, K. R. Chan, M. Loewenstein, M. H. Proffitt, and B. L. Gary, 1996: Stratospheric horizontal wavenumber spectra of winds, potential temperature, and atmospheric tracers observed by high-altitude aircraft. *J. Geophys. Res.*, **101**, 9441–9470, doi:10.1029/95JD03835.

Bierdel, L., P. Friederichs, and S. Bentzien, 2012: Upscale error growth in a high-resolution simulation of a summertime weather event over Europe. *Meteor. Z.*, **21**, 245–258, doi:10.1127/0941-2948/2012/0319.

Blažica, V., N. Gustafsson, and N. Žagar, 2015: The impact of periodization methods on the kinetic energy spectra for limited-area numerical weather prediction models. *Geosci. Model Dev.*, **8**, 87–97, doi:10.5194/gmd-8-87-2015.

Bryan, G. H., J. C. Wyngaard, and J. M. Fritsch, 2003: Resolution requirements for the simulation of deep moist convection. *Mon. Wea. Rev.*, **131**, 2394–2416, doi:10.1175/1520-0493(2003)131<2394:RRFTSO>2.0.CO;2.

Carbone, R. E., J. D. Tuttle, D. A. Ahijevych, and S. B. Trier, 2002: Inferences of predictability associated with warm season precipitation episodes. *J. Atmos. Sci.*, **59**, 2033–2056, doi:10.1175/1520-0469(2002)059<2033:IOPAWW>2.0.CO;2.

Cho, J. Y. N., and E. Lindborg, 2001: Horizontal velocity structure functions in the upper troposphere and lower stratosphere: 1. Observations. *J. Geophys. Res.*, **106**, 10 223–10 232, doi:10.1029/2000JD900814.

Crane, R. K., 1990: Space-time structure of rain rate fields. *J. Geophys. Res.*, **95**, 2011–2020, doi:10.1029/JD095iD03p02011.

Davis, C., B. Brown, and R. Bullock, 2006: Object-based verification of precipitation forecasts. Part I: Methodology and application to mesoscale rain areas. *Mon. Wea. Rev.*, **134**, 1772–1784, doi:10.1175/MWR3145.1.

Errico, R. M., 1985: Spectra computed from a limited area grid. *Mon. Wea. Rev.*, **113**, 1554–1562, doi:10.1175/1520-0493(1985)113<1554:SCFALA>2.0.CO;2.

Gilleland, E., D. Ahijevych, B. G. Brown, B. Casati, and E. E. Ebert, 2009: Intercomparison of spatial forecast verification methods. *Wea. Forecasting*, **24**, 1416–1430, doi:10.1175/2009WAF2222269.1.

Grell, G. A., and S. R. Freitas, 2014: A scale and aerosol aware stochastic convective parameterization for weather and air quality modeling. *Atmos. Chem. Phys.*, **14**, 5233–5250, doi:10.5194/acp-14-5233-2014.

Hamilton, K., Y. O. Takahashi, and W. Ohfuchi, 2008: Mesoscale spectrum of atmospheric motions investigated in a very fine resolution global general circulation model. *J. Geophys. Res.*, **113**, D18110, doi:10.1029/2008JD009785.

Harris, D., E. Foufoula-Georgiou, K. K. Droegemeier, and J. J. Levit, 2001: Multiscale statistical properties of a high-resolution precipitation forecast. *J. Hydrometeor.*, **2**, 406–418, doi:10.1175/1525-7541(2001)002<0406:MSPOAH>2.0.CO;2.

Harris, F. J., 1978: On the use of windows for harmonic analysis with the discrete Fourier transform. *Proc. IEEE*, **66**, 51–83, doi:10.1109/PROC.1978.10837.

Hinkelman, L. M., B. Stevens, and K. F. Evans, 2005: A large-eddy simulation study of anisotropy in fair-weather cumulus cloud fields. *J. Atmos. Sci.*, **62**, 2155–2171, doi:10.1175/JAS3463.1.

——, K. F. Evans, E. E. Clothiaux, T. P. Ackerman, and P. W. Stackhouse Jr., 2007: The effect of cumulus cloud field anisotropy on domain-averaged solar fluxes and atmospheric heating rates. *J. Atmos. Sci.*, **64**, 3499–3520, doi:10.1175/JAS4032.1.

Hong, S. Y., and J. Lim, 2006: The WRF single-moment 6-class microphysics scheme (WSM6). *J. Korean Meteor. Soc.*, **42**, 129–151.

Horn, L. H., and R. A. Bryson, 1963: An analysis of the geostrophic kinetic energy spectrum of large-scale atmospheric turbulence. *J. Geophys. Res.*, **68**, 1059–1064, doi:10.1029/JZ068i004p01059.

Iacono, M. J., E. J. Mlawer, and S. A. Clough, 2000: Impact of an improved longwave radiation model, RRTM, on the energy budget and thermodynamic properties of the NCAR Community Climate Model, CCM3. *J. Geophys. Res.*, **105**, 14 873–14 890, doi:10.1029/2000JD900091.

Janjić, Z. I., 1994: The step-mountain eta coordinate model: Further developments of the convection, viscous sublayer, and turbulence closure schemes. *Mon. Wea. Rev.*, **122**, 927–945, doi:10.1175/1520-0493(1994)122<0927:TSMECM>2.0.CO;2.

——, 2002: Nonsingular implementation of the Mellor–Yamada level 2.5 scheme in the NCEP Meso model. NCEP Office Note 437, 61 pp.

Jolliffe, I. T., and D. B. Stephenson, 2003: *Forecast Verification: A Practitioner's Guide in Atmospheric Science.* Wiley, 240 pp.

Julian, P. R., W. M. Washington, L. Hembree, and C. Ridley, 1970: On the spectral distribution of large-scale atmospheric kinetic energy. *J. Atmos. Sci.*, **27**, 376–387, doi:10.1175/1520-0469(1970)027<0376:OTSDOL>2.0.CO;2.

Knievel, J. C., G. H. Bryan, and J. P. Hacker, 2007: Explicit numerical diffusion in the WRF model. *Mon. Wea. Rev.*, **135**, 3808–3824, doi:10.1175/2007MWR2100.1.

Langhans, W., J. Schmidli, and C. Schär, 2012: Mesoscale impacts of explicit numerical diffusion in a convection-permitting model. *Mon. Wea. Rev.*, **140**, 226–244, doi:10.1175/2011MWR3650.1.

Lin, Y., and K. E. Mitchell, 2005: The NCEP stage II/IV hourly precipitation analyses: Development and applications. *19th Conf. on Hydrology*, San Diego, CA, Amer. Meteor. Soc., 1.2.

[Available online at https://ams.confex.com/ams/Annual2005/techprogram/paper_83847.htm.]

Mellor, G. L., and T. Yamada, 1982: Development of a turbulence closure model for geophysical fluid problems. *Rev. Geophys. Space Phys.*, **20**, 851–875, doi:10.1029/RG020i004p00851.

Menabde, M., A. Seed, D. Harris, and G. Austin, 1999: Multiaffine random field model of rainfall. *Water Resour. Res.*, **35**, 509–514, doi:10.1029/1998WR900020.

Mlawer, E. J., S. J. Taubman, P. D. Brown, M. J. Iacono, and S. A. Clough, 1997: Radiative transfer for inhomogeneous atmospheres: RRTM, a validated correlated-k model for the longwave. *J. Geophys. Res.*, **102**, 16 663–16 682, doi:10.1029/97JD00237.

Morales, J. E., and G. Poveda, 2009: Diurnally driven scaling properties of Amazonian rainfall fields: Fourier spectra and order-q statistical moments. *J. Geophys. Res.*, **114**, D11104, doi:10.1029/2008JD011281.

Nakanishi, M., and H. Niino, 2009: Development of an improved turbulence closure model for the atmospheric boundary layer. *J. Meteor. Soc. Japan*, **87**, 895–912, doi:10.2151/jmsj.87.895.

Nastrom, G. D., and K. S. Gage, 1985: A climatology of atmospheric wavenumber spectra of wind and temperature observed by commercial aircraft. *J. Atmos. Sci.*, **42**, 950–960, doi:10.1175/1520-0469(1985)042<0950:ACOAWS>2.0.CO;2.

——, ——, and W. H. Jasperson, 1984: Kinetic energy spectrum of large-and mesoscale atmospheric processes. *Nature*, **310**, 36–38, doi:10.1038/310036a0.

Parodi, A., E. Foufoula-Georgiou, and K. Emanuel, 2011: Signature of microphysics on spatial rainfall statistics. *J. Geophys. Res.*, **116**, D14119, doi:10.1029/2010JD015124.

Ricard, D., C. Lac, S. Riette, R. Legrand, and A. Mary, 2013: Kinetic energy spectra characteristics of two convection-permitting limited-area models AROME and Meso-NH. *Quart. J. Roy. Meteor. Soc.*, **139**, 1327–1341, doi:10.1002/qj.2025.

Roberts, N. M., and H. W. Lean, 2008: Scale-selective verification of rainfall accumulations from high-resolution forecasts of convective events. *Mon. Wea. Rev.*, **136**, 78–97, doi:10.1175/2007MWR2123.1.

Schwartz, C. S., G. S. Romine, R. A. Sobash, K. R. Fossell, and M. L. Weisman, 2015: NCAR's experimental real-time convection-allowing ensemble prediction system. *Wea. Forecasting*, **30**, 1645–1654, doi:10.1175/WAF-D-15-0103.1.

Skamarock, W. C., 2004: Evaluating mesoscale NWP models using kinetic energy spectra. *Mon. Wea. Rev.*, **132**, 3019–3032, doi:10.1175/MWR2830.1.

——, and Coauthors, 2008: A description of the Advanced Research WRF version 3. NCAR Tech. Note NCAR/TN-475+STR, 113 pp., doi:10.5065/D68S4MVH.

——, J. B. Klemp, M. G. Duda, L. D. Fowler, S.-H. Park, and T. D. Ringler, 2012: A multiscale nonhydrostatic atmospheric model using centroidal Voronoi tesselations and C-grid staggering. *Mon. Wea. Rev.*, **140**, 3090–3105, doi:10.1175/MWR-D-11-00215.1.

——, S.-H. Park, J. B. Klemp, and C. Snyder, 2014: Atmospheric kinetic energy spectra from global high-resolution nonhydrostatic simulations. *J. Atmos. Sci.*, **71**, 4369–4381, doi:10.1175/JAS-D-14-0114.1.

Stephan, C., and M. J. Alexander, 2015: Realistic simulations of atmospheric gravity waves over the continental U.S. using precipitation radar data. *J. Adv. Model. Earth Syst.*, **7**, 823–835, doi:10.1002/2014MS000396.

Terasaki, K., H. L. Tanaka, and M. Satoh, 2009: Characteristics of the kinetic energy spectrum of NICAM model atmosphere. *SOLA*, **5**, 180–183, doi:10.2151/sola.2009-046.

Thompson, G., P. R. Field, R. M. Rasmussen, and W. D. Hall, 2008: Explicit forecasts of winter precipitation using an improved bulk microphysics scheme. Part II: Implementation of a new snow parameterization. *Mon. Wea. Rev.*, **136**, 5095–5115, doi:10.1175/2008MWR2387.1.

Tiedtke, M., 1989: A comprehensive mass flux scheme for cumulus parameterization in large-scale models. *Mon. Wea. Rev.*, **117**, 1779–1800, doi:10.1175/1520-0493(1989)117<1779:ACMFSF>2.0.CO;2.

Tuttle, J. D., and C. A. Davis, 2006: Corridors of warm season precipitation in the central United States. *Mon. Wea. Rev.*, **134**, 2297–2317, doi:10.1175/MWR3188.1.

Wiin-Nielsen, A., 1967: On the annual variation and spectral distribution of atmospheric energy. *Tellus*, **19A**, 540–559, doi:10.1111/j.2153-3490.1967.tb01507.x.

Wilks, D. S., 2011: *Statistical Methods in the Atmospheric Sciences.* 3rd ed. Academic Press, 704 pp.

Willeit, M., R. Amorati, A. Montani, V. Pavan, and M. S. Tesini, 2015: Comparison of spectral characteristics of precipitation from radar estimates and COSMO-model predicted fields. *Meteor. Atmos. Phys.*, **127**, 191–203, doi:10.1007/s00703-014-0359-8.

Wilson, J. W., and E. A. Brandes, 1979: Radar measurement of rainfall—A summary. *Bull. Amer. Meteor. Soc.*, **60**, 1048–1058, doi:10.1175/1520-0477(1979)060<1048:RMORS>2.0.CO;2.

Zhang, C., Y. Wang, and K. Hamilton, 2011: Improved representation of boundary layer clouds over the Southeast Pacific in ARW-WRF using a modified Tiedtke cumulus parameterization scheme. *Mon. Wea. Rev.*, **139**, 3489–3513, doi:10.1175/MWR-D-10-05091.1.

Zhang, J., Y. Qi, C. Langston, B. Kaney, and K. Howard, 2014: A real-time algorithm for merging radar QPEs with rain gauge observations and orographic precipitation climatology. *J. Hydrometeor.*, **15**, 1794–1809, doi:10.1175/JHM-D-13-0163.1.

——, and Coauthors, 2016: Multi-Radar Multi-Sensor (MRMS) quantitative precipitation estimation: Initial operating capabilities. *Bull. Amer. Meteor. Soc.*, **97**, 621–638, doi:10.1175/BAMS-D-14-00174.1.